Color Image Super Resolution in Real Noise

Srimanta Mandal*
DA-IICT
Gandhinagar, Gujarat
in.srimanta.mandal@ieee.org

Kuldeep Purohit
IIT Madras
Chennai, Tamil Nadu
kuldeeppurohit3@gmail.com

A. N. Rajagopalan
IIT Madras
Chennai, Tamil Nadu
raju@ee.iitm.ac.in

ABSTRACT

In practice, images can contain different amounts of noise for different color channels, which is not acknowledged by existing super-resolution approaches. In this paper, we propose to super-resolve noisy color images by considering the color channels jointly. Noise statistics are blindly estimated from the input low-resolution image and are used to assign different weights to different color channels in the data cost. Implicit low-rank structure of visual data is enforced via nuclear norm minimization in association with adaptive weights, which is added as a regularization term to the cost. Additionally, multi-scale details of the image are added to the model through another regularization term that involves projection onto PCA basis, which is constructed using similar patches extracted across different scales of the input image. The results demonstrate the super-resolving capability of the approach in real scenarios.

CCS CONCEPTS

• **Computing methodologies** → **Reconstruction**; *Image processing*; Regularization;

KEYWORDS

Real Color Image, Noise, Super Resolution, Nuclear Norm, PCA

ACM Reference Format:
Srimanta Mandal, Kuldeep Purohit, and A. N. Rajagopalan. 2018. Color Image Super Resolution in Real Noise. In *11th Indian Conference on Computer Vision, Graphics and Image Processing (ICVGIP 2018), December 18–22, 2018, Hyderabad, India,* Anoop M. Namboodiri, Vineeth Balasubramanian, Amit Roy-Chowdhury, and Guido Gerig (Eds.). ACM, New York, NY, USA, Article 61, 9 pages. https://doi.org/10.1145/3293353.3293414

1 INTRODUCTION

Imaging systems are susceptible to noise in different conditions. Low light imaging requires higher analog gain (ISO value) of a camera, responsible for noise inclusion in the imaged scene [35]. Now-a-days, majority of the images are captured by smartphone cameras as compared to the point-and-shoot and DSLR cameras. However, the ease of photography with smartphone often comes with the cost of higher levels of noise owing to smaller size of sensors [1]. Further, the captured images can be lower in resolution, which may not fulfill the requirement of different HD applications. Thus, it becomes necessary to recover a noise less high resolution (HR) image from the captured noisy low resolution (LR) image.

The LR image formation process can be represented mathematically as

$$\mathbf{y} = \mathbf{DHx} + \mathbf{n}, \tag{1}$$

where $\mathbf{y} \in \Re^N$ is the LR observation, which is generated from the blurred (by $\mathbf{H} \in \Re^{M \times M}$ matrix) and decimated (by $\mathbf{D} \in \Re^{N \times M}$ matrix) version of the HR scene $\mathbf{x} \in \Re^M$ with an additive noise $\mathbf{n} \in \Re^N$ ($M > N$). This mathematical model is devised from the imaging pipeline, where decimation happens due to limited size of the sensors [33]. The objective of super resolution (SR) is to achieve an estimation of $\mathbf{x}$ from $\mathbf{y}$, and is an ill-posed one as the number of unknowns (M) exceeds the number of equations (N). Further, the presence of $\mathbf{n}$ increases the perplexity of the problem.

The ill-posed objective can be partially accomplished using existing super resolution (SR) techniques [9, 10, 29, 40, 45]. As the high frequency (HF) information often gets attenuated or degraded in the imaging process, the SR approaches involve incorporating high frequency information. This is generally imported either from sub-pixel shifted multiple LR target images or from example images with HF content. Further, the ill-posed nature is often subjugated by prior information such as total-variation, non-local similarity, sparsity, etc. [9, 27, 29, 31]. Absence of example image database or multiple LR images of the target scene with sub-pixel shift criteria can make these kinds of SR approaches paralyzed. Such scenario can be addressed by utilizing the intra/inter-scale patch similarity [11, 25, 27, 39, 42, 44]. In the inverse process, presence of noise often plays as a malefactor. Only a few approaches of SR are reported in the literature that works in noisy situation [27, 28, 39]. Furthermore, unknown statistics of noise can make the restoration more difficult [27, 28].

The existing approaches consider only the luminance component for SR by neglecting the color information [9, 27, 28, 41, 47]. However, in real scenario, noise can be present in different amounts in different color channels [15, 17, 23, 32, 43]. This is because different channels have different ISO sensitivities. Further, the relative sensitivities vary with different WB settings. Thus, super-resolving the luminance component may not be able to handle the channel varying noise. One strategy could be to apply SR algorithms separately on each of the color channels. However, distinct processing of each color channel disregards the correlation among channels.

In this paper, we propose to super-resolve a real noisy color image by considering the color channels jointly to explore the correlation among the color channels. Further, different weights are assigned to different color channels in the data cost in order to address the channel varying noise. The weights are estimated using the noise statistics from each channel. The low-rank property of clean data is approximated by incorporating weighted nuclear

*The work has been done during his post-doctoral studies at IPCV Lab, IIT Madras

ICVGIP 2018, December 18–22, 2018, Hyderabad, India

ACM ISBN 978-1-4503-6615-1/18/12…$15.00
https://doi.org/10.1145/3293353.3293414

norm. Though, the nuclear norm minimization strategy has been employed in SR by the work [28], it minimizes the nuclear norm uniformly without considering the significance of different singular values. Further, the approach [28] super-resolves the luminance component only. Whereas, we consider the significance of different singular values by adaptively weighting them, as weighted nuclear norm minimization can restore an image better than uniform minimization [12]. Moreover, the spectral correlation is utilized by considering all the color channels jointly with adaptive weights. Multi-scale image details are embraced in the formulation by augmenting another regularization term that involves projection onto PCA basis, learned from inter-scale similar RGB patches.

Here our main assumption is that the noise of real color image in standard RGB (sRGB) space can be approximated by the multivariate Gaussian model, as demonstrated in [32]. Other noise such as Poisson may not be well suppressed by our approach, however presence of other additive noise can be adequately addressed.

Rest of the paper is sequenced as follows: Section 2 discusses some of the related works, and highlights the contributions. The noise statistics are analyzed for real color images in Section 3, where the proposed approach of weighted data cost and nuclear norm minimization is elaborated along with PCA based constraint. The approach is evaluated for real noisy color images using standard datasets in Section 4. Finally, the conclusion is drawn in Section 5.

2 RELATED WORKS

The advent of SR techniques was started with multiple sub-pixel shifted LR images of the scene [33]. Different sub-pixel shifted images are assumed to provide different view points of the same scene. Hence, combining different view points can complement each other to produce an HR image [40]. Providing enough number of images, the under-determined problem becomes determined to solve for the unknowns, and produce HR image. Further, these set of approaches are numerically limited to smaller factors [11]. Additionally, the requirement of large number of images became hindrance for such approaches. Hence, the focus of research has shifted towards single image SR approaches, where the requirement of multiple LR images of the target scene is replaced with the requirement of some HR example images [10]. The assumption behind such approaches is that the missing HF information of LR images can be imported from HR example set. However, processing multiple HR images increases the memory requirement. Thus, patch based processing has been adopted for SR [9, 41, 45, 47].

Absence of patches similar to the target patch in the database increases the complexity of the problem. This scenario can be addressed by including prior information about the image. Natural image statistics such as smoothness prior has often been used in terms of Tikhonov, total variation, Markov random field, etc. [16, 31, 48]. Among the other priors, non-local similarity and sparsity inducing norms are the notable ones. Non-local similarity explores the patch similarity that are not constrained to a local region [9, 11, 24]. Sparsity inducing norm has been employed in SR approaches on the basis that natural image is sparse in some domain [9, 27, 46, 47]. While using sparsity inducing norm, the target patch is generally represented by linear combination of few patches from the database of patches, represented as columns of an over-complete matrix, known as dictionary [2, 26, 29]. Dictionary can have analytic form such as DCT or it can be learned from example patches [2, 29, 36, 45]. Sparsity prior has often been combined with others such as non-local self similarity to improve SR performance [8]. Most of these approaches will not work in the scenario when example images are unavailable. Moreover, these approaches do not consider channel varying noise in the models.

Surge of recent deep learning techniques has inspired researchers to employ deep convolutional neural network (CNN) for SR [6, 7]. Since then, different CNN architectures have been employed for SR. Residual network [13] has been used to create deeper framework in conjunction with skip connection and recursive convolution to improve the results [18, 19]. Nested skip connection has also been engaged with encoder-decoder architecture to improve convergence [30]. Most of these approaches appraise bicubic interpolated version of the LR image as input to the network [6, 18, 19]. Processing a higher dimensional image for very large number of levels requires higher computational resources. In order to avoid such condition, up-sampling module has been appended at the end of the network [7, 21, 37]. However, these approaches can not deal with different scales [18]. VDSR [18] has capability of training joint SR for different scales, and produce superior results than scale-specific network with the cost of higher computational burden. This requirement has been mitigated by using ResNet architecture in the SRResNet model [21]. The ResNet architecture was originally proposed for different higher level vision tasks [13]. Hence, direct application of it to SR may not be optimal. An optimized and simplified version of the SRResNet has been proposed via EDSR to improve the results [22]. To accommodate multiple scales, MDSR proposed a multi-scale architecture that shares the set of parameters across different scales [22]. The performance of all these deep learning based approaches depends on availability of large number of example images. Moreover, the training-testing condition for these methods needs to be same.

In order to alleviate such hard restrictions, small image-specific CNN has been developed based on patch recurrences in the input image [38]. The patch recurrence concept has also been explored by some traditional approaches [11, 14, 25, 39, 42, 44]. These methods super-resolve the given LR image based on the presumption that the HF information can be found out from similar patches across different scales. However, most of these techniques ignore the correlation among the color channels. Further, the presence of noise in the LR image has often been neglected in the model.

The task of SR from a noisy LR image has been performed by a few techniques [27, 28, 39]. The approach [39] poses the problem as a combination of denoising and SR. The noisy LR image is super resolved directly to produce an HR version, which is conjugated with another HR image, derived from denoised LR image in order to produce the final HR result. The motivation behind the method is that the denoised LR image often lacks the HF information, which can be imported from the super-resolved noisy HR image. The main drawback of it is that the performance depends on the denoising algorithm. This issue has been taken care by implicit denoising while performing SR by the approach [27]. This method estimates few parameters that are related to the noise statistics and are used in considering non-local mean or detail component for further processing. However, the approach [27] considers only the luminance

component for SR. Thus, it can not take care of the channel varying noise. This holds true for the approach [28], which applies nuclear norm minimization on luminance channel. In contrast, we jointly super resolve the color channels by considering different weights for different channels. Moreover, we consider weighted nuclear norm regularization to prioritize the significant singular values. Further, the solution is regularized by including a constraint that includes multi-scale image details through projection onto PCA basis.

The contributions of the proposed approach are summarized as follows:

- We propose to super-resolve color images in real noise by considering color channels jointly.
- Different weights for different channels are estimated from their noise statistics, which are derived blindly from the input LR image. The estimated weights are used in the data cost.
- Nuclear norm minimization is employed with adaptive weights, which are assigned based on significance of singular values. The weighted nuclear norm forms a regularization term in our cost.
- Multi-scale image details are augmented in the model as another regularization term based on PCA and the combined objective function is optimized using ADMM algorithm.

3 PROPOSED APPROACH

We analyze noise statistics for color images in real noise to demonstrate it's channel varying nature. This behavior is included in constructing the data cost function, which is assisted with weighted nuclear norm and PCA basis based regularization term to model the problem. The entire cost function is optimized using alternating direction method of multipliers [3].

3.1 Inter-Channel Noise Statistics

In order to check the behavior of noise across color channels, we estimate the noise variances for real images using the technique [4]. The real images are obtained from [20]. The noise variances are shown in bar plots for different real examples in Fig. 1. Note that the noise variances are not same across channels. Further, the variations across channels are also not uniform. Hence, depending on scenes, the *red, green & blue* channels will be affected differently. Thus, processing only luminance component of the image or applying SR on every channel uniformly may not be suitable for all images. This urges for an SR approach that takes care of the issue, which we are going to discuss next.

3.2 Model Formulation

For a color image, the eq. (1) can be re-written as

$$\mathbf{y}_l = \mathbf{D}\mathbf{H}\mathbf{x}_l + \mathbf{n}_l, \quad l \in \{r, g, b\}. \tag{2}$$

The objective is to recover $\mathbf{x}_l$ for each of the *red, green & blue* channels, represented by r, g, b. In order to proceed, the LR color image is up-sampled by off-the-shelf interpolation technique to achieve an initial HR approximation, i.e., $\hat{\mathbf{x}}_l = (\mathbf{y}_l) \uparrow_d$. Patches are extracted in overlapping manner from the initial version as $\mathbf{x}_{i,l} = \mathbf{P}_i \hat{\mathbf{x}}_l$, where $\mathbf{P}_i$ extracts i^{th} patch $\mathbf{x}_{i,l} \in \Re^m$ from l^{th} color channel. Now, the patches from each of the color channels are stacked together to form a vector $\mathbf{x}_i = [\mathbf{x}_{i,r}; \mathbf{x}_{i,g}; \mathbf{x}_{i,b}] \in \Re^{3m}$. For each of these patches, we search for similarity in the image in terms of l_2 distance, and select s similar patches. These are kept in column-wise mode to form a matrix $\mathbf{X}_i \in \Re^{3m \times s}$.

In order to remove the bias of DC value, we extract detail component by subtracting a weighted mean from the matrix $\mathbf{X}_i$ as

$$\mathbf{X}_{i,r} = \mathbf{X}_i - \mathbf{X}_{i,m}, \tag{3}$$

where, $\mathbf{X}_{i,m}$ is the weighted mean of similar patches, and is estimated as

$$\mathbf{X}_{i,m} = \mathcal{R}\left[\sum_{j=1}^{s}\left\{\frac{1}{z}\exp\left(-\frac{||\mathbf{x}_i - \mathbf{x}_j||_2^2}{h}\right)\right\}\mathbf{x}_j\right]. \tag{4}$$

$\mathcal{R}$ repeats the vector to form a matrix of size equal to $\mathbf{X}_i$. z is normalizing constant, and h controls the decay of the exponential.

Consider $\boldsymbol{\mathcal{X}}_i$ is the clean HR counterpart of $\mathbf{X}_i$. Since, $\boldsymbol{\mathcal{X}}_i$ will have similar clean patches, the rank of it will be lesser. It follows that the rank of $\boldsymbol{\mathcal{X}}_{i,r}$ will also be lower. By defining rank as number of non-zero singular values i.e., $\mathcal{K}\left(\boldsymbol{\mathcal{X}}_{i,r}\right) = \sum_k ||\sigma_k\left(\boldsymbol{\mathcal{X}}_{i,r}\right)||_0$, we can minimize the rank along with a data cost that imposes the data continuity as

$$\hat{\boldsymbol{\mathcal{X}}}_{i,r} = \arg\min_{\boldsymbol{\mathcal{X}}_{i,r}}\left\{||\mathbf{X}_{i,r} - \boldsymbol{\mathcal{X}}_{i,r}||_F^2 + \mathcal{K}\left(\boldsymbol{\mathcal{X}}_{i,r}\right)\right\}. \tag{5}$$

Solving above equation involves l_0 norm minimization, which is NP-hard in nature. Thus rank is often relaxed as $\sum_k ||\sigma_k\left(\boldsymbol{\mathcal{X}}_{i,r}\right)||_1$, which is also known as nuclear norm $||\boldsymbol{\mathcal{X}}_{i,r}||_*$ [12]. Hence, eq. (5) can be re-written as

$$\hat{\boldsymbol{\mathcal{X}}}_{i,r} = \arg\min_{\boldsymbol{\mathcal{X}}_{i,r}}\left\{||\mathbf{X}_{i,r} - \boldsymbol{\mathcal{X}}_{i,r}||_F^2 + ||\boldsymbol{\mathcal{X}}_{i,r}||_*\right\}. \tag{6}$$

In order to tackle the channel varying noise, we include a weight matrix $\boldsymbol{\Lambda}$ in the data term. Further, above equation minimizes all the singular values uniformly, irrespective of their significance. Considering the importance of different singular values, we assign weights to minimize them differently [12]. The weighted nuclear norm can be written as

$$||\boldsymbol{\mathcal{X}}_{i,r}||_{w,*} = \sum_k ||w_k\sigma_k\left(\boldsymbol{\mathcal{X}}_{i,r}\right)||_1 = \sum_k w_k\sigma_k\left(\boldsymbol{\mathcal{X}}_{i,r}\right) \tag{7}$$

Thus, with the weights, the eq. (6) can be written as

$$\hat{\boldsymbol{\mathcal{X}}}_{i,r} = \arg\min_{\boldsymbol{\mathcal{X}}_{i,r}}\left\{||\boldsymbol{\Lambda}\mathbf{X}_{i,r} - \boldsymbol{\Lambda}\boldsymbol{\mathcal{X}}_{i,r}||_F^2 + ||\boldsymbol{\mathcal{X}}_{i,r}||_{w,*}\right\}. \tag{8}$$

3.2.1 The Weight $\boldsymbol{\Lambda}$: The weights $\boldsymbol{\Lambda}$ can be estimated using a MAP framework, where we want to maximize the probability of $\boldsymbol{\mathcal{X}}_{i,r}$, given $\mathbf{X}_{i,r}$ and w.

$$\begin{aligned}\hat{\boldsymbol{\mathcal{X}}}_{i,r} &= \arg\max_{\boldsymbol{\mathcal{X}}_{i,r}}\left\{\ln P\left(\boldsymbol{\mathcal{X}}_{i,r}|\mathbf{X}_{i,r}, w\right)\right\} \\ &= \arg\min_{\boldsymbol{\mathcal{X}}_{i,r}}\left\{-\ln P\left(\boldsymbol{\mathcal{X}}_{i,r}|\mathbf{X}_{i,r}, w\right)\right\} \\ &= \arg\min_{\boldsymbol{\mathcal{X}}_{i,r}}\left\{-\ln P\left(\mathbf{X}_{i,r}|\boldsymbol{\mathcal{X}}_{i,r}\right) - \ln P\left(\boldsymbol{\mathcal{X}}_{i,r}|w\right)\right\}\end{aligned} \tag{9}$$

Here, the term $P\left(\mathbf{X}_{i,r}|\boldsymbol{\mathcal{X}}_{i,r}\right)$ is approximated by the noise statistics. According to our observation from Fig. 1, we can assume that noise

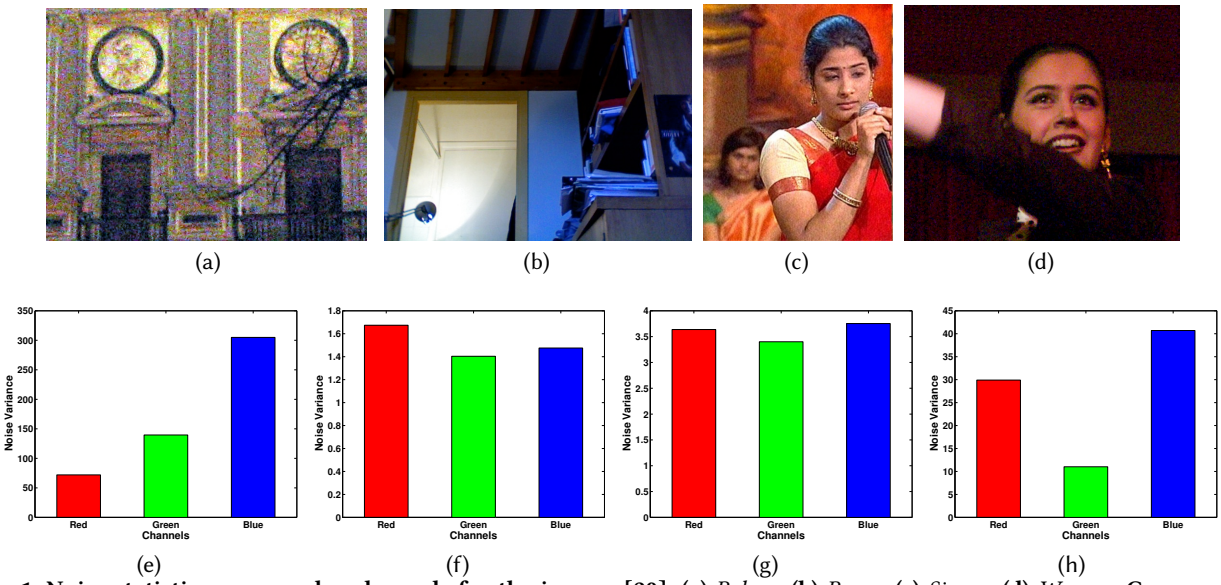

Figure 1: Noise statistics across color channels for the images [20]: (a) *Palace*; **(b)** *Room*; **(c)** *Singer*; **(d)** *Woman*. **Corresponding variances of noise for different channels are shown in (e-h), respectively.**

is independent and identically distributed across channel. Further, the distribution can be assumed to be Gaussian [32]. Hence,

$$P\left(\mathbf{X}_{i,r}|\boldsymbol{\mathcal{X}}_{i,r}\right) = \prod_{l} \frac{1}{\left(2\pi\sigma_l^2\right)^{\frac{3m}{2}}} \exp\left(-\frac{1}{2\sigma_l^2}||\mathbf{X}_{i,r,l} - \boldsymbol{\mathcal{X}}_{i,r,l}||_F^2\right). \quad (10)$$

The weighted nuclear norm is acted on $\boldsymbol{\mathcal{X}}_{i,r}$. Hence, the term $P\left(\boldsymbol{\mathcal{X}}_{i,r}|w\right)$ will be proportional to $\exp\left(-\frac{1}{2}||\boldsymbol{\mathcal{X}}_{i,r}||_{w,*}\right)$. Putting these two terms in eq. (9), we get

$$\hat{\boldsymbol{\mathcal{X}}}_{i,r} = \arg\min_{\boldsymbol{\mathcal{X}}_{i,r}} \sum_{l} \frac{1}{\sigma_l^2}||\mathbf{X}_{i,r,l} - \boldsymbol{\mathcal{X}}_{i,r,l}||_F^2 + ||\boldsymbol{\mathcal{X}}_{i,r}||_{w,*}. \quad (11)$$

This can be further written as

$$\hat{\boldsymbol{\mathcal{X}}}_{i,r} = \arg\min_{\boldsymbol{\mathcal{X}}_{i,r}} \sum_{l} ||\frac{1}{\sigma_l}\mathbf{X}_{i,r,l} - \frac{1}{\sigma_l}\boldsymbol{\mathcal{X}}_{i,r,l}||_F^2 + ||\boldsymbol{\mathcal{X}}_{i,r}||_{w,*}. \quad (12)$$

Comparing, eq. (12) with eq. (8), we can write the weight matrix $\boldsymbol{\Lambda} \in \Re^{3m\times 3m}$ as a diagonal matrix, whose non-zero entries are $1/\sigma_l$.

3.2.2 The Weight w: The weight w is assigned according to the significance of the singular values. For natural images, the larger singular values represents more important information than the smaller ones. Hence, the larger singular values should be penalized lesser than the smaller singular values. Thus, one natural choice is to take inverse of the singular values in some proportion. Here, we choose w as [12]

$$w_k = \frac{C}{\sigma_k\left(\boldsymbol{\mathcal{X}}_{i,r}\right) + \epsilon}, \quad (13)$$

where $\sigma_k\left(\boldsymbol{\mathcal{X}}_{i,r}\right)$ is the k^{th} singular value of $\boldsymbol{\mathcal{X}}_{i,r}$, C and ϵ are constants.

3.3 Employing Multi-Scale Image Details

Here, we bring out the multi-scale image details in form of PCA basis. For a target patch $\mathbf{x}_i \in \Re^{3m}$, we find its similar patches across scales. The similar patches extracted from different up-scaled versions as well as down-scaled versions can provide the required patch details to generate HR patch. This is because we perceive a coarser view of a scene from a long distance, and details of the scene reveal gradually when we approach towards it. These similar patches are gathered together in a column-wise manner to generate a matrix $\mathbf{T}_i$, which is mean subtracted to unveil the details of different scales. The mean subtracted matrix $\mathbf{T}_{i,r}$ is then used to find eigenvectors, which are further arranged in descending order corresponding to eigenvalues and placed in a matrix $\mathbf{B}_i$, which forms the required basis.

The information, embedded in basis $\mathbf{B}_i$ is included into our formulation in form of a regularization term. Precisely, we project $\mathbf{X}_{i,r}$ onto $\mathbf{B}_i$, and revert it back via soft-thresholding and multiplication with basis. This should be closer to the the matrix $\boldsymbol{\mathcal{X}}_{i,r}$. Thus, the eq. (12) is modified with the new term as

$$\begin{aligned}\hat{\boldsymbol{\mathcal{X}}}_{i,r} \quad = \quad & \arg\min_{\boldsymbol{\mathcal{X}}_{i,r}} \left\{||\boldsymbol{\Lambda}\left(\mathbf{X}_{i,r} - \boldsymbol{\mathcal{X}}_{i,r}\right)||_F^2 + ||\boldsymbol{\mathcal{X}}_{i,r}||_{w,*}\right. \\ & \left. + ||\boldsymbol{\mathcal{X}}_{i,r} - \mathbf{B}_i\boldsymbol{\mathcal{S}}\left(\mathbf{B}_i^T\mathbf{X}_{i,r}\right)_\alpha||_F^2\right\}, \end{aligned} \quad (14)$$

where, $\boldsymbol{\mathcal{S}}\left(\cdot\right)_\alpha$ is a soft thresholding operator that shrinks the larger projection coefficients towards the center, and smaller coefficients to zero based on threshold α.

3.4 Optimization

Unfortunately, the problem of eq. (14) does not have a closed form solution because of the weight matrix $\boldsymbol{\Lambda}$ and the soft thresholding operator $\boldsymbol{\mathcal{S}}$. In order to solve the equation, we introduce an augmented variable $\boldsymbol{\mathcal{F}}$, which is used to represent the equation as a linear equality-constrained problem using variable splitting method.

To simplify expressions, in the optimization steps, we remove the subscripts of the variables. For example, $\boldsymbol{\mathcal{X}}_{i,r}$ will be represented as $\boldsymbol{\mathcal{X}}$. Hence, the cost can be written as

$$\min_{\boldsymbol{\mathcal{X}},\boldsymbol{\mathcal{F}}} ||\boldsymbol{\Lambda}(\mathbf{X}-\boldsymbol{\mathcal{X}})||_F^2 + ||\boldsymbol{\mathcal{X}} - \mathbf{B}\boldsymbol{\mathcal{S}}\left(\mathbf{B}^T\mathbf{X}\right)_\alpha||_F^2 + ||\boldsymbol{\mathcal{F}}||_{w,*} \quad s.t.\ \ \boldsymbol{\mathcal{X}} = \boldsymbol{\mathcal{F}}. \tag{15}$$

The eq. (15) is separable, hence it can be solved by alternating direction method of multipliers (ADMM) [3]. The augmented Lagrangian function becomes

$$\mathcal{L}(\boldsymbol{\mathcal{X}},\boldsymbol{\mathcal{F}},\boldsymbol{\Gamma},\rho) = ||\boldsymbol{\Lambda}(\mathbf{X}-\boldsymbol{\mathcal{X}})||_F^2 + ||\boldsymbol{\mathcal{X}} - \mathbf{B}\boldsymbol{\mathcal{S}}\left(\mathbf{B}^T\mathbf{X}\right)_\alpha||_F^2 + ||\boldsymbol{\mathcal{F}}||_{w,*} + \langle\boldsymbol{\Gamma}, \boldsymbol{\mathcal{X}}-\boldsymbol{\mathcal{F}}\rangle + \frac{\rho}{2}||\boldsymbol{\mathcal{X}}-\boldsymbol{\mathcal{F}}||_F^2, \tag{16}$$

where $\boldsymbol{\Gamma}$ is the augmented Lagrangian multiplier, and ρ is the penalty parameter. We denote $\boldsymbol{\mathcal{X}}_k$, $\boldsymbol{\mathcal{F}}_k$ and $\boldsymbol{\Gamma}_k$ are the optimization variables and Lagrangian multiplier at k^{th} iteration. Initialization of the variables are done by assigning zero matrices to $\boldsymbol{\mathcal{X}}_0$, $\boldsymbol{\mathcal{F}}_0$ and $\boldsymbol{\Gamma}_0$. The penalty parameter is assigned a small positive value. By taking derivative of the augmented Lagrangian function with respect to $\boldsymbol{\mathcal{X}}$ & $\boldsymbol{\mathcal{F}}$, and equating it to zero, we can update the variables in following manner:

(1) Update $\boldsymbol{\mathcal{X}}$:

$$\boldsymbol{\mathcal{X}}_{k+1} = \arg\min_{\boldsymbol{\mathcal{X}}} ||\boldsymbol{\Lambda}(\mathbf{X}-\boldsymbol{\mathcal{X}})||_F^2 + ||\boldsymbol{\mathcal{X}} - \mathbf{B}\boldsymbol{\mathcal{S}}\left(\mathbf{B}^T\mathbf{X}\right)_\alpha||_F^2 + \frac{\rho_k}{2}||\boldsymbol{\mathcal{X}} - \boldsymbol{\mathcal{F}}_k + \rho_k^{-1}\boldsymbol{\Gamma}_k||_F^2. \tag{17}$$

This has a closed form solution:

$$\boldsymbol{\mathcal{X}}_{k+1} = \left(\boldsymbol{\Lambda}^T\boldsymbol{\Lambda} + \mathbf{I} + \frac{\rho_k}{2}\mathbf{I}\right)^{-1}\left(\boldsymbol{\Lambda}^T\boldsymbol{\Lambda}\mathbf{X} + \mathbf{B}\boldsymbol{\mathcal{S}}\left(\mathbf{B}^T\mathbf{X}\right)_\alpha + \frac{\rho_k}{2}\boldsymbol{\mathcal{F}}_k - \boldsymbol{\Gamma}_k\right). \tag{18}$$

The soft-thresholding operator $\boldsymbol{\mathcal{S}}$ is defined as

$$\boldsymbol{\mathcal{S}}\left(\mathbf{B}^T\mathbf{X}\right)_\alpha = sign\left(\mathbf{B}^T\mathbf{X}\right)\left(|\mathbf{B}^T\mathbf{X}| - \alpha\right)_+, \tag{19}$$

where $\left(|\mathbf{B}^T\mathbf{X}| - \alpha\right)_+$ is established as

$$\left(|\mathbf{B}^T\mathbf{X}| - \alpha\right)_+ = \begin{cases} 0 & \text{if } |\mathbf{B}^T\mathbf{X}| < \alpha \\ |\mathbf{B}^T\mathbf{X}| - \alpha & \text{if } |\mathbf{B}^T\mathbf{X}| > \alpha \end{cases} \tag{20}$$

(2) Update $\boldsymbol{\mathcal{F}}$:

$$\boldsymbol{\mathcal{F}}_{k+1} = \arg\min_{\boldsymbol{\mathcal{F}}} \frac{\rho_k}{2}||\boldsymbol{\mathcal{F}} - \left(\boldsymbol{\mathcal{X}}_{k+1} + \rho_k^{-1}\boldsymbol{\Gamma}_k\right)||_F^2 + ||\boldsymbol{\mathcal{F}}||_{w,*} \tag{21}$$

Let SVD of $\left(\boldsymbol{\mathcal{X}}_{k+1} + \rho_k^{-1}\boldsymbol{\Gamma}_k\right) = \mathbf{U}_k\Sigma_k\mathbf{V}_k^T$. According to eq. (13), the weights are inversely proportional to the singular values. It follows that $0 \le w_1 \le w_2 \cdots \le w_n$. The work [12] suggests that the above form of equation has a closed form solution for non-decreasing weights and the solution is

$$\boldsymbol{\mathcal{F}}_{k+1} = \mathbf{U}_k\boldsymbol{\mathcal{S}}(\Sigma_k)_{\frac{w_k}{2}}\mathbf{V}_k^T. \tag{22}$$

(3) Update $\boldsymbol{\Gamma}$:

$$\boldsymbol{\Gamma}_{k+1} = \boldsymbol{\Gamma}_k + \rho_k(\boldsymbol{\mathcal{X}}_{k+1} - \boldsymbol{\mathcal{F}}_{k+1}) \tag{23}$$

(4) Update ρ:

$$\rho_{k+1} = \eta * \rho_k \ \text{ where } \eta > 1 \tag{24}$$

These steps are repeated until the algorithm converges or reaches the maximum number of iterations.

3.5 Obtaining the Final Result

The solution $\boldsymbol{\mathcal{X}}_{i,r}$ is added with $\mathbf{X}_{i,m}$ of eq. (4) to get the colored version $\hat{\mathbf{X}}_i$. Columns of $\hat{\mathbf{X}}_i$ contains the super-resolved patches similar to $\mathbf{x}_i$. In this manner, all the patches are super-resolved ($\hat{\mathbf{x}}_{i,l}$), and are stitched together to form a full image $\hat{\hat{\mathbf{x}}}_l$. Extracted patches from the full image should be consistent with the restored patches $\hat{\mathbf{x}}_{i,l}$. Further, the recovered HR image should be harmonious with the input image, if down-sampled in same way. We need to get solution, which follows above two constraints, and can be achieved by solving

$$\hat{\hat{\mathbf{x}}}_l = \arg\min_{\hat{\hat{\mathbf{x}}}_l}\left\{\sum_i ||\mathbf{P}_i\hat{\hat{\mathbf{x}}}_l - \hat{\mathbf{x}}_{i,l}||_2^2 + \beta\,||\mathbf{y}_l - \mathbf{D}\mathbf{H}\hat{\hat{\mathbf{x}}}_l||_2^2\right\}. \tag{25}$$

The first term recovers the entire image for each color channel from the recovered patches, and the second term is data continuity term. A closed form solution can be derived from eq. (25)

$$\hat{\hat{\mathbf{x}}}_l = \left(\sum_i \mathbf{P}_i^T\mathbf{P}_i + \beta\,\mathbf{H}^T\mathbf{D}^T\mathbf{D}\mathbf{H}\right)^{-1}\left(\sum_i \mathbf{P}_i^T\hat{\mathbf{x}}_{i,l} + \beta\,\mathbf{H}^T\mathbf{D}^T\mathbf{y}_l\right). \tag{26}$$

The recovered $\hat{\hat{\mathbf{x}}}_l$ for each color channel can be spliced together to produce the final color image.

4 EXPERIMENTAL RESULTS

We evaluate the proposed approach by considering real images as provided by [20, 32]. The dataset [32] is created by capturing images of 11 static scenes under controlled indoor environment using different cameras with different settings. However, a camera and its settings are kept fixed for shooting a particular scene. In this manner, 500 images per scene are captured. The mean of these images can serve as ground truth for each of the scenes and can be used for computing quantitative measurements such as PSNR, and SSIM. Originally, dimensions of the captured images are quite large (of the order 7000×5000). However, 15 cropped versions of the images with dimension 512×512 are provided by the authors of [32]. These 15 smaller images are used in our approach for experimentation. In contrast, the dataset [20] is constructed in uncontrolled environment. A set of 20 images of different dimensions are considered from the dataset [20] for experimental purpose. Absence of ground truths in the dataset restricts us to do only visual comparison.

The noisy images are down-sampled by factor 3 using MATLAB command *imresize* with *bicubic* interpolation to generate LR images. The noise statistics for each color channels are estimated from the LR images using [4]. The LR image is then up-scaled using bicubic interpolation technique to generate an initial approximation of HR image. Patches of size 6×6 are extracted from the initial HR image. For each patch, we search for its similarity in 25×25 neighborhood and consider 20 most similar patches. To accommodate image details in the model, we sample the initial HR image into 6 different levels by factors $(0.8)^i$, where $i = 1, 2, 3, 4, 5, 6$. The initial value of ρ is set to be 1. The α for soft-thresholding operator is chosen as 0.8. The maximum iterations are limited to 360. The computational complexity of this approach is $O(m^3L)$, where m is

the size of a patch, and L is the number of patches. We have compared our results with various approaches including conventional approaches [9, 27, 28, 34, 41, 45, 47] as well as deep learning based approaches[6, 22, 38].

4.1 Experiments Using Dataset [32]

The quantitative measures such as PSNR and SSIM[1] for the results on 15 images of the dataset [32] are depicted in Table 1 along with the results of existing approaches. Among these approaches, RP[45], ASDS[9], SU[47], SRCNN[6], Aplus[41], SPSR[34], EDSR[22] depends on example image patches. However, NASR[27], NNSR[28], and ZSSR[38] do not require example image patches. It can be observed from the table that for most of the cases, we are able to produce the best results, as denoted by bold fonts. Further, the superiority of our approach can be verified visually through an example, as shown in Fig.2. From first glance, the results appear to be more or less similar. However, difference can be found in the zoomed in part of the image. The example image based approaches [6, 9, 22, 34, 41, 47] are not able to reduce the noisy artifacts much as they have not seen images with real noise and their ground truths in the training set. Further, these approaches do not model the noise with its channel varying characteristic. Though, NASR [27] can take care of the noise but the channel varying nature of it restricts the method from performing well, as can be observed in (f). On the other side, ZSSR [38] is a deep learning based approach, which over-fits on the given LR image to produce an SR result, which is still infected by noise. Whereas, we are able to reduce the noisy artifacts due to the elegant combination of weighted data cost, weighted nuclear norm and multi-scale image details.

4.2 Experiments Using Dataset [20]

This dataset does not contain any ground truth of the noisy observations. Hence, the computation of the metrics PSNR & SSIM are not possible for the dataset. Here, we show the results of different approaches along with the results of our method in Fig. 3. One can observe that existing approaches including the deep learning ones are not able to reduce the noisy artifacts. Further, the edges of some of their results are smeared. However, our approach is able to suppress the effect of noise without smearing the edges. Similar improvement can be observed in Fig. 4, where we have considered a scene, captured in dim lighting condition. The image is contaminated with real noise due to higher ISO. However, our approach is able to produce better results as can be seen in the zoomed-in parts. This improvement is due to the cultivated combination of different regularization terms along with weighted data cost.

4.3 Comparisons with Denoising+SR Approaches

Here we compare the results of our approach with the existing SR approaches, where the LR images are first denoised as a preprocessing step of SR. CBM3D [5] has been considered for the denoising purpose. For comparisons, we consider a few SR approaches that cover different types of methodologies including a sparse representation based [34], regression based [41], and deep

[1]PSNR values are positioned above the SSIM values in each cell of the table.

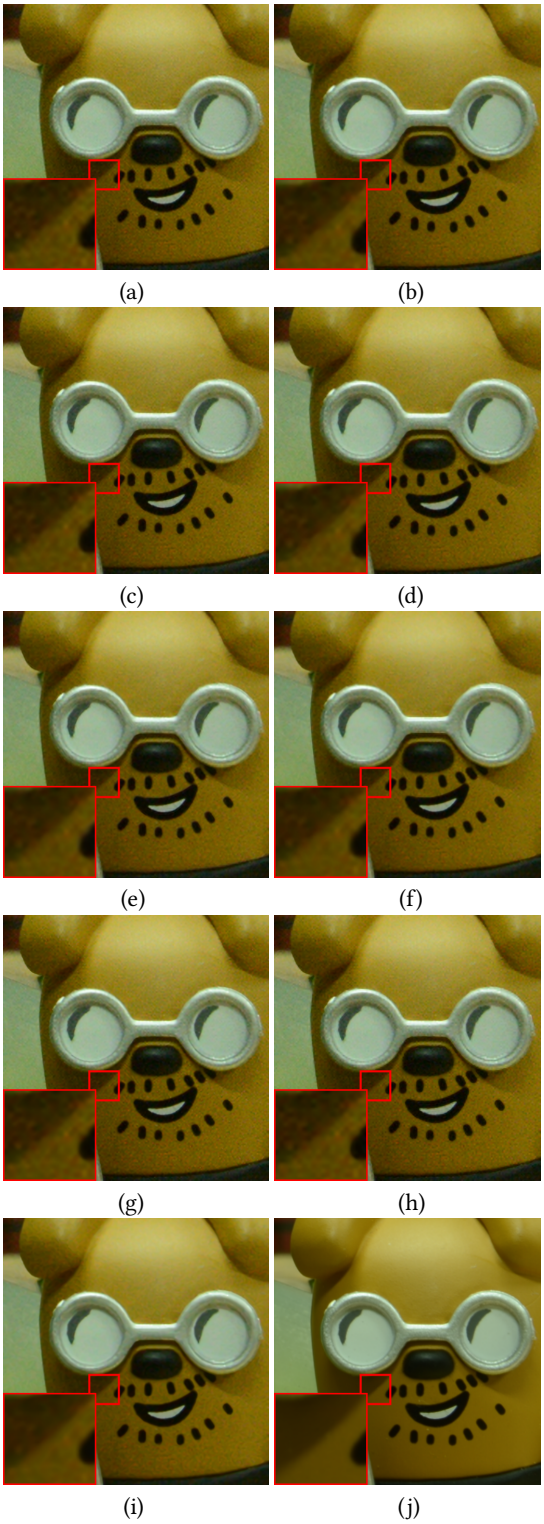

Figure 2: Visual results on 1^{st} scene of Nikon D800 (ISO = 3200) from Table 1. (a)-(i) depict the results of ASDS[9], SU[47], SRCNN[6], A+[41], SPSR[34], NASR[27], EDSR[22], ZSSR[38], & our result, respectively; (j) represents the Ground truth.

Table 1: Results of SR on dataset [32](↑ 3)

Camera	RP[45]	ASDS[9]	SU[47]	SRCN[6]	A+[41]	SPSR[34]	NASR[27]	EDSR[22]	NNSR[28]	ZSSR[38]	ours
	40.35	40.70	41.15	40.81	41.12	41.38	40.91	41.40	40.92	40.52	**41.65**
	0.9684	0.9644	0.9694	0.9655	0.9676	0.9720	0.9726	0.9691	0.9727	0.9654	**0.9741**
Nikon D800	37.05	37.22	37.78	38.13	37.40	35.57	37.95	37.98	**39.46**	36.82	38.78
ISO = 1600	0.9761	0.9640	0.9694	0.9658	0.9652	0.9678	0.9754	0.9677	**0.9810**	0.9614	0.9785
	40.68	40.20	40.64	40.25	40.59	40.88	41.06	40.74	41.47	39.36	**41.49**
	0.9619	0.9506	0.9574	0.9520	0.9551	0.9616	0.9641	0.9560	0.9651	0.9468	**0.9657**
	40.95	39.43	39.96	39.46	39.73	40.53	40.60	39.78	41.55	39.66	**41.75**
	0.9760	0.9468	0.9579	0.9487	0.9518	0.9642	0.9660	0.9511	0.9700	0.9472	**0.9752**
Nikon D800	39.83	40.17	40.61	40.29	40.42	40.89	40.42	40.66	37.38	39.67	**41.39**
ISO = 3200	0.9676	0.9627	0.9683	0.9638	0.9653	0.9710	0.9649	0.9664	0.9589	0.9627	**0.9747**
	40.62	39.27	40.07	39.35	39.53	40.86	40.92	39.53	42.13	39.25	**42.53**
	0.9320	0.9255	0.9416	0.9278	0.9309	0.9529	0.9540	0.9308	0.9683	0.9276	**0.9700**
	35.81	36.85	36.46	38.43	36.76	37.39	38.22	**39.64**	38.40	35.74	39.50
	0.9494	0.9620	0.9654	0.9667	0.9684	0.9724	0.9702	0.9753	0.9753	0.9590	**0.9807**
Cannon 5D	35.78	36.38	36.26	36.57	36.55	36.57	36.87	**37.41**	35.38	35.42	37.11
ISO = 3200	0.9408	0.9411	0.9433	0.9424	0.9440	0.9485	0.9464	0.9532	0.9417	0.9317	**0.9546**
	35.93	37.84	37.61	37.09	37.68	37.32	**38.46**	38.10	38.17	36.48	37.92
	0.9588	0.9648	0.9660	0.9618	0.9648	0.9672	**0.9716**	0.9676	0.9700	0.9575	0.9687
	36.47	37.54	37.49	37.16	37.41	37.58	**38.25**	37.75	37.80	37.93	37.65
	0.9599	0.9648	0.9663	0.9631	0.9643	0.9687	**0.9718**	0.9684	0.9688	0.9628	0.9687
Nikon D600	37.37	38.23	38.03	38.01	38.11	38.10	**39.47**	38.62	39.24	37.67	39.00
ISO = 3200	0.9679	0.9644	0.9682	0.9644	0.9660	0.9709	0.9752	0.9683	**0.9756**	0.9610	0.9750
	40.96	39.88	40.80	40.29	40.53	40.78	39.08	40.66	39.56	40.36	**41.27**
	0.9841	0.9656	0.9735	0.9675	0.9691	0.9771	0.9754	0.9698	0.9810	0.9653	**0.9841**
	34.14	33.78	33.97	34.03	33.87	34.10	35.79	34.93	**36.15**	33.74	35.49
	0.9184	0.8682	0.8881	0.8733	0.8764	0.8970	0.9153	0.8832	**0.9281**	0.8691	0.9226
Nikon D800	34.79	35.05	35.21	35.08	35.24	35.39	35.57	35.49	35.82	35.07	**36.00**
ISO = 6400	0.9416	0.9238	0.9334	0.9264	0.9285	0.9383	0.9455	0.9299	0.9403	0.9230	**0.9500**
	35.31	34.91	35.40	35.02	35.21	35.51	35.28	35.39	34.67	34.12	**36.21**
	0.9219	0.9023	0.9167	0.9059	0.9087	0.9192	0.9093	0.9110	0.9136	0.8926	**0.9330**
Average	37.74	37.86	38.10	38.00	38.08	38.19	38.59	38.54	38.54	37.45	**39.18**
	0.9550	0.9447	0.9523	0.9463	0.9484	0.9566	0.9585	0.9512	0.9618	0.9422	**0.9650**

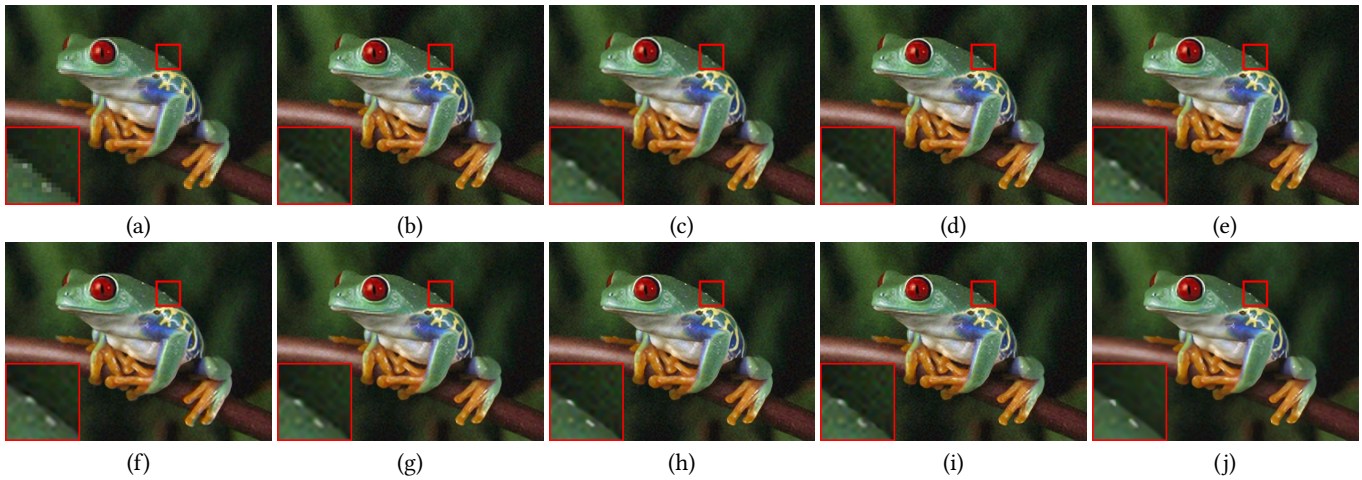

Figure 3: Visual results on *Frog* from the dataset [20]. (a) shows the LR image, (b)-(j) depict the results of ASDS[9], SU[47], SRCNN[6], A+[41], SPSR[34], NASR[27], EDSR[22], ZSSR[38], and our result, respectively.

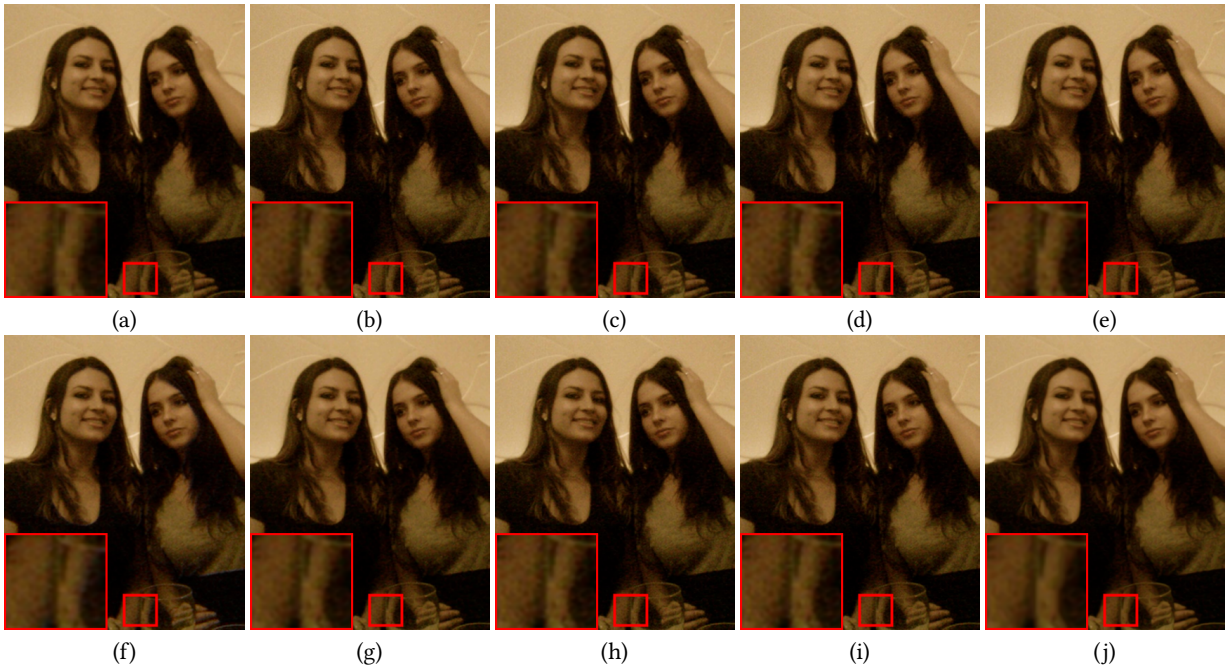

Figure 4: Visual results on *Girls* from the dataset [20]. (a) shows the LR image, (b)-(j) depict the results of ASDS[9], SU[47], SRCNN[6], A+[41], SPSR[34], NASR[27], EDSR[22], ZSSR[38], and our result, respectively.

Table 2: Results of Denoising+SR on dataset [32](↑ 3)

Average Metrics	CBM3D[5]+ A+[41]	CBM3D[5]+ SPSR[34]	CBM3D[5]+ ZSSR[38]	ours
PSNR	35.44	35.35	38.62	**39.18**
SSIM	0.9509	0.9479	0.9643	**0.9650**

learning based [38]. The average PSNR & SSIM metrics for these approaches along with ours are tabulated in Table 2 for the dataset [32]. Note that for our approach, we use the original noisy LR images as input. One can observe that the proposed approach is able to out-perform these denoising [5]+SR approaches. The reason being that the denoising approach CBM3D consider processing each channel separately by considering uniform noise statistic across channels, which is calculated as $\sigma = \sqrt{\left(\sigma_r^2 + \sigma_b^2 + \sigma_b^2\right)}/3$. Here σ_r, σ_g, and σ_b are estimated using[4]. As a consequence, some of the channels may become over-smoothed and some becomes under-smoothed. Hence, the final results may pose some artifacts. The example based approaches [34, 41] are not trained to suppress those, hence their performance degrades. However, the ZSSR [38] method explores the patch recurrent concept which helps in reducing the artifacts up to some extent. Thus, the performance of ZSSR has improved. However, the improvement has come by using denoising and SR approaches sequentially. On contrary, our method considers channel-varying noise statistic along with weighted nuclear norm and multi-level-details in a single framework to produce superior results.

5 CONCLUSION

We proposed to super-resolve an image in real noise by alleviating the channel varying noise of it. Weights, adaptive to the noise statistics were assigned to the data cost, which was augmented by two regularization terms. One of the terms maintains the low-rank property of similar patches by weighted nuclear norm minimization, where weight carries the significance of singular values. Multi-scale image details were embedded into the model through the second regularization term, which was constructed via projection onto PCA basis. The combined objective function was minimized using ADMM-based optimization algorithm, which leads to suppression of noise while bringing out image details. The results demonstrated the super-resolving capability of our approach in real noise.

ACKNOWLEDGMENTS

The work is supported by the Indian Institute of Technology Madras under Grant No.: IRA1415004RESFANRA for Prof. A.N. Rajagopalan under Institute Research and Development Mid Career Level Award.

REFERENCES

[1] Abdelrahman Abdelhamed, Stephen Lin, and Michael S. Brown. 2018. A High-Quality Denoising Dataset for Smartphone Cameras. In *IEEE Conference on Computer Vision and Pattern Recognition (CVPR)*. 1692–1700.
[2] M. Aharon, M. Elad, and A. Bruckstein. Nov. 2006. K-SVD: An Algorithm for Designing Overcomplete Dictionaries for Sparse Representation. *IEEE Transactions on Signal Processing* 54, 11 (Nov. 2006), 4311–4322.
[3] Stephen Boyd, Neal Parikh, Eric Chu, Borja Peleato, and Jonathan Eckstein. 2011. Distributed Optimization and Statistical Learning via the Alternating Direction Method of Multipliers. *Found. Trends Mach. Learn.* 3, 1 (Jan. 2011), 1–122. https://doi.org/10.1561/2200000016
[4] G. Chen, F. Zhu, and P. A. Heng. 2015. An Efficient Statistical Method for Image Noise Level Estimation. In *IEEE International Conference on Computer Vision (ICCV)*. 477–485. https://doi.org/10.1109/ICCV.2015.62
[5] K. Dabov, A. Foi, V. Katkovnik, and K. Egiazarian. 2007. Color Image Denoising via Sparse 3D Collaborative Filtering with Grouping Constraint in Luminance-Chrominance Space. In *IEEE International Conference on Image Processing (ICIP)*, Vol. 1. I – 313–I – 316. https://doi.org/10.1109/ICIP.2007.4378954

[6] Chao Dong, ChenChange Loy, Kaiming He, and Xiaoou Tang. 2014. Learning a Deep Convolutional Network for Image Super-Resolution. In *Computer Vision – ECCV 2014*. Lecture Notes in Computer Science, Vol. 8692. Springer International Publishing, 184–199. https://doi.org/10.1007/978-3-319-10593-2_13

[7] Chao Dong, Chen Change Loy, and Xiaoou Tang. 2016. Accelerating the Super-Resolution Convolutional Neural Network. In *Computer Vision – ECCV 2016*, Bastian Leibe, Jiri Matas, Nicu Sebe, and Max Welling (Eds.). Springer International Publishing, Cham, 391–407.

[8] W. Dong, L. Zhang, G. Shi, and X. Li. 2013. Nonlocally Centralized Sparse Representation for Image Restoration. *IEEE Transactions on Image Processing* 22, 4 (April 2013), 1620–1630. https://doi.org/10.1109/TIP.2012.2235847

[9] Weisheng Dong, Lei Zhang, Guangming Shi, and Xiaolin Wu. 2011. Image Deblurring and Super-Resolution by Adaptive Sparse Domain Selection and Adaptive Regularization. *IEEE Transactions on Image Processing* 20, 7 (Jul. 2011), 1838 –1857. https://doi.org/10.1109/TIP.2011.2108306

[10] W.T. Freeman, T.R. Jones, and E.C. Pasztor. 2002. Example-based super-resolution. *IEEE, Computer Graphics and Applications* 22, 2 (mar/apr 2002), 56 –65. https://doi.org/10.1109/38.988747

[11] D. Glasner, S. Bagon, and M. Irani. 2009. Super-resolution from a single image. In *IEEE International Conference on Computer Vision (ICCV)*. 349–356. https://doi.org/10.1109/ICCV.2009.5459271

[12] Shuhang Gu, Qi Xie, Deyu Meng, Wangmeng Zuo, Xiangchu Feng, and Lei Zhang. 2017. Weighted Nuclear Norm Minimization and Its Applications to Low Level Vision. *International Journal of Computer Vision* 121, 2 (01 Jan 2017), 183–208. https://doi.org/10.1007/s11263-016-0930-5

[13] K. He, X. Zhang, S. Ren, and J. Sun. 2016. Deep Residual Learning for Image Recognition. In *IEEE Conference on Computer Vision and Pattern Recognition (CVPR)*. 770–778. https://doi.org/10.1109/CVPR.2016.90

[14] J. B. Huang, A. Singh, and N. Ahuja. 2015. Single image super-resolution from transformed self-exemplars. In *IEEE Conference on Computer Vision and Pattern Recognition (CVPR)*. 5197–5206. https://doi.org/10.1109/CVPR.2015.7299156

[15] G. Jeon and E. Dubois. 2013. Demosaicking of Noisy Bayer-Sampled Color Images With Least-Squares Luma-Chroma Demultiplexing and Noise Level Estimation. *IEEE Transactions on Image Processing* 22, 1 (Jan 2013), 146–156. https://doi.org/10.1109/TIP.2012.2214041

[16] Atsunori Kanemura, Shin ichi Maeda, and Shin Ishii. 2009. Superresolution with compound Markov random fields via the variational {EM} algorithm. *Neural Networks* 22, 7 (2009), 1025 – 1034. https://doi.org/10.1016/j.neunet.2008.12.005

[17] Hakki Can Karaimer and Michael S. Brown. 2016. A Software Platform for Manipulating the Camera Imaging Pipeline. In *Computer Vision – ECCV*, Bastian Leibe, Jiri Matas, Nicu Sebe, and Max Welling (Eds.). Springer International Publishing, Cham, 429–444.

[18] J. Kim, J. K. Lee, and K. M. Lee. 2016. Accurate Image Super-Resolution Using Very Deep Convolutional Networks. In *IEEE Conference on Computer Vision and Pattern Recognition (CVPR)*. 1646–1654. https://doi.org/10.1109/CVPR.2016.182

[19] J. Kim, J. K. Lee, and K. M. Lee. 2016. Deeply-Recursive Convolutional Network for Image Super-Resolution. In *2016 IEEE Conference on Computer Vision and Pattern Recognition (CVPR)*. 1637–1645. https://doi.org/10.1109/CVPR.2016.181

[20] Marc Lebrun, Miguel Colom, and Jean-Michel Morel. 2015. The Noise Clinic: a Blind Image Denoising Algorithm. *Image Processing On Line* 5 (2015), 1–54. https://doi.org/10.5201/ipol.2015.125

[21] C. Ledig, L. Theis, F. Huszár, J. Caballero, A. Cunningham, A. Acosta, A. Aitken, A. Tejani, J. Totz, Z. Wang, and W. Shi. 2017. Photo-Realistic Single Image Super-Resolution Using a Generative Adversarial Network. In *IEEE Conference on Computer Vision and Pattern Recognition (CVPR)*. 105–114. https://doi.org/10.1109/CVPR.2017.19

[22] B. Lim, S. Son, H. Kim, S. Nah, and K. M. Lee. 2017. Enhanced Deep Residual Networks for Single Image Super-Resolution. In *IEEE Conference on Computer Vision and Pattern Recognition Workshops (CVPRW)*. 1132–1140. https://doi.org/10.1109/CVPRW.2017.151

[23] C. Liu, R. Szeliski, S. Bing Kang, C. L. Zitnick, and W. T. Freeman. 2008. Automatic Estimation and Removal of Noise from a Single Image. *IEEE Transactions on Pattern Analysis and Machine Intelligence* 30, 2 (Feb 2008), 299–314. https://doi.org/10.1109/TPAMI.2007.1176

[24] J. Mairal, F. Bach, J. Ponce, G. Sapiro, and A. Zisserman. 2009. Non-local sparse models for image restoration. In *IEEE 12th International Conference on Computer Vision*. 2272 –2279. https://doi.org/10.1109/ICCV.2009.5459452

[25] S. Mandal, A. Bhavsar, and A.K. Sao. 2014. Super-resolving a Single Intensity/Range Image via Non-local Means and Sparse Representation. In *Indian Conference on Computer Vision, Graphics and Image Processing (ICVGIP), 2014*. 1–8. https://doi.org/10.1145/2683483.2683541

[26] S. Mandal, A. Bhavsar, and A. K. Sao. 2017. Depth Map Restoration From Undersampled Data. *IEEE Transactions on Image Processing* 26, 1 (Jan 2017), 119–134. https://doi.org/10.1109/TIP.2016.2621410

[27] Srimanta Mandal, Arnav Bhavsar, and Anil Kumar Sao. 2017. Noise adaptive super-resolution from single image via non-local mean and sparse representation. *Signal Processing* 132 (2017), 134 – 149. https://doi.org/10.1016/j.sigpro.2016.09.017

[28] Srimanta Mandal and A. N. Rajagopalan. 2018. Single Noisy Image Super Resolution by Minimizing Nuclear Norm in Virtual Sparse Domain. In *Computer Vision, Pattern Recognition, Image Processing, and Graphics*, Renu Rameshan, Chetan Arora, and Sumantra Dutta Roy (Eds.). Springer Singapore, Singapore, 163–176.

[29] Srimanta Mandal and Anil Kumar Sao. 2016. Employing structural and statistical information to learn dictionary(s) for single image super-resolution in sparse domain. *Signal Processing: Image Communication* 48 (2016), 63 – 80. https://doi.org/10.1016/j.image.2016.08.006

[30] Xiao-Jiao Mao, Chunhua Shen, and Yu-Bin Yang. 2016. Image Restoration Using Very Deep Convolutional Encoder-decoder Networks with Symmetric Skip Connections. In *Proceedings of the 30th International Conference on Neural Information Processing Systems (NIPS'16)*. Curran Associates Inc., USA, 2810–2818. http://dl.acm.org/citation.cfm?id=3157382.3157412

[31] Antonio Marquina and Stanley J. Osher. 2008. Image Super-Resolution by TV-Regularization and Bregman Iteration. *Journal of Scientific Computing* 37 (2008), 367–382. Issue 3. https://doi.org/10.1007/s10915-008-9214-8

[32] S. Nam, Y. Hwang, Y. Matsushita, and S. J. Kim. 2016. A Holistic Approach to Cross-Channel Image Noise Modeling and Its Application to Image Denoising. In *IEEE Conference on Computer Vision and Pattern Recognition (CVPR)*. 1683–1691. https://doi.org/10.1109/CVPR.2016.186

[33] Sung Cheol Park, Min Kyu Park, and Moon Gi Kang. 2003. Super-resolution image reconstruction: a technical overview. *IEEE, Signal Processing Magazine* 20, 3 (may 2003), 21 – 36. https://doi.org/10.1109/MSP.2003.1203207

[34] T. Peleg and M. Elad. 2014. A Statistical Prediction Model Based on Sparse Representations for Single Image Super-Resolution. *IEEE Transactions on Image Processing* 23, 6 (June 2014), 2569–2582. https://doi.org/10.1109/TIP.2014.2305844

[35] T. Plötz and S. Roth. 2017. Benchmarking Denoising Algorithms with Real Photographs. In *IEEE Conference on Computer Vision and Pattern Recognition (CVPR)*. 2750–2759. https://doi.org/10.1109/CVPR.2017.294

[36] R. Rubinstein, A.M. Bruckstein, and M. Elad. 2010. Dictionaries for Sparse Representation Modeling. *Proc. IEEE* 98, 6 (june 2010), 1045 –1057. https://doi.org/10.1109/JPROC.2010.2040551

[37] W. Shi, J. Caballero, F. Huszár, J. Totz, A. P. Aitken, R. Bishop, D. Rueckert, and Z. Wang. 2016. Real-Time Single Image and Video Super-Resolution Using an Efficient Sub-Pixel Convolutional Neural Network. In *IEEE Conference on Computer Vision and Pattern Recognition (CVPR)*. 1874–1883. https://doi.org/10.1109/CVPR.2016.207

[38] Assaf Shocher, Nadav Cohen, and Michal Irani. 2018. "Zero-Shot" Super-Resolution Using Deep Internal Learning. In *The IEEE Conference on Computer Vision and Pattern Recognition (CVPR)*. 3118–3126.

[39] A. Singh, F. Porikli, and N. Ahuja. 2014. Super-resolving Noisy Images. In *IEEE Conference on Computer Vision and Pattern Recognition (CVPR)*. 2846–2853. https://doi.org/10.1109/CVPR.2014.364

[40] Henry Stark and Peyma Oskoui. 1989. High-resolution image recovery from image-plane arrays, using convex projections. *J. Opt. Soc. Am. A* 6, 11 (Nov. 1989), 1715–1726.

[41] Radu Timofte, Vincent De Smet, and Luc Van Gool. 2015. A+: Adjusted Anchored Neighborhood Regression for Fast Super-Resolution. In *Computer Vision – ACCV 2014*. Lecture Notes in Computer Science, Vol. 9006. Springer International Publishing, 111–126. https://doi.org/10.1007/978-3-319-16817-3_8

[42] S. Vishnukumar, Madhu S. Nair, and M. Wilscy. 2014. Edge preserving single image super-resolution with improved visual quality. *Signal Processing* 105, 0 (2014), 283 – 297. https://doi.org/10.1016/j.sigpro.2014.05.033

[43] J. Xu, L. Zhang, D. Zhang, and X. Feng. 2017. Multi-channel Weighted Nuclear Norm Minimization for Real Color Image Denoising. In *IEEE International Conference on Computer Vision (ICCV)*. 1105–1113. https://doi.org/10.1109/ICCV.2017.125

[44] Chih-Yuan Yang, Jia-Bin Huang, and Ming-Hsuan Yang. 2011. Exploiting Self-similarities for Single Frame Super-Resolution. In *Computer Vision – ACCV 2010*, Ron Kimmel, Reinhard Klette, and Akihiro Sugimoto (Eds.). Lecture Notes in Computer Science, Vol. 6494. Springer Berlin Heidelberg, 497–510. https://doi.org/10.1007/978-3-642-19318-7_39

[45] Jianchao Yang, J. Wright, T. Huang, and Yi Ma. Jun. 2008. Image super-resolution as sparse representation of raw image patches. In *IEEE Conference on Computer Vision and Pattern Recognition*. 1–8. https://doi.org/10.1109/CVPR.2008.4587647

[46] Jianchao Yang, J. Wright, T.S. Huang, and Yi Ma. Nov. 2010. Image Super-Resolution Via Sparse Representation. *IEEE Transactions on Image Processing* 19, 11 (Nov. 2010), 2861–2873. https://doi.org/10.1109/TIP.2010.2050625

[47] Roman Zeyde, Michael Elad, and Matan Protter. 2012. On Single Image Scale-Up Using Sparse-Representations. In *Curves and Surfaces*. Vol. 6920. Springer, 711–730. https://doi.org/10.1007/978-3-642-27413-8_47

[48] Xin Zhang, EdmundY. Lam, EdX. Wu, and KennethK.Y. Wong. 2008. Application of Tikhonov Regularization to Super-Resolution Reconstruction of Brain MRI Images. In *Medical Imaging and Informatics*, Xiaohong Gao, Henning Müller, MartinJ. Loomes, Richard Comley, and Shuqian Luo (Eds.). Lecture Notes in Computer Science, Vol. 4987. Springer Berlin Heidelberg, 51–56. https://doi.org/10.1007/978-3-540-79490-5_8